PAPER

Check for updates

Scalable and environmentally friendly MXene-tetrahedrites for next-generation flexible thermoelectrics†

Priyanshu Banerjee,‡[a] Jiyuan Huang,‡[a] Jacob Lombardo,[a] Swapnil B. Ambade,[b] Rohan B. Ambade,[cdef] Tae Hee Han, [ID][cd] Srushti Kulkarni,[a] Shreyasi Sengupta, [ID][g] Zeev Rosenzweig, [ID][g] Howard Fairbrother, [ID][b] Sichao Li, [ID][h] Sunmi Shin [ID][h] and Deepa Madan [ID] *[a]

Traditional thermoelectric generators (TEGs) face scalability challenges due to high-temperature, long-duration curing processes and rare-earth/toxic chalcogenides such as bismuth telluride. Additive manufacturing has been investigated as a more time-, energy- and cost-efficient method that offers greater flexibility than traditional manufacturing techniques. Additionally, tetrahedrites are promising thermoelectric materials in high-temperature applications because they are non-toxic and earth-abundant. Herein, this work demonstrates the fabrication of scalable and sustainable $Cu_{12}Sb_4S_{13}$ (CAS) based composite films and flexible TEG devices (f-TEGs) with 2D MXene nanosheets using a low-thermal budget additive manufacturing approach for room temperature applications. 2D MXene nanosheets introduced energy-barrier scattering and nanoscale features to effectively increase the room-temperature ZT to 0.22, 10% higher than bulk CAS, by decoupling electrical conductivity, Seebeck coefficient, and thermal conductivity. CAS and 2D MXenes were found to be environmentally safe through a bacterial viability study. The process is used to create a 5-leg f-TEG device producing a power of 5.3 μW and a power density of 140 μW cm^{-2} at a ΔT of 25 K. Therefore, this work demonstrates that combining scalable and sustainable materials and methods is an effective strategy for high-performance room-temperature f-TEGs that could potentially harvest the low waste heat energy of the human body.

1 Introduction

Thermoelectric generators (TEGs) are alternative energy harvesting technologies that convert waste heat into electrical power through the Seebeck effect. TEGs have gained attention due to their potential to harness lost heat energy and are expected to play a crucial role in future wearable health monitoring devices.[1] Current battery technology cannot meet the needs of wearable devices that provide continuous health monitoring (blood sugar, heart rate, *etc.*) due to prolonged periods of recharging and significant device downtime. Integrating additional power sources into wearables is challenging, with bulky batteries and tethered power sources not ideal due to their impact on aesthetics and comfort. A cost-effective, sustainable, and efficient solution that could be easily incorporated into existing wearable designs that prolong device usage and minimize downtime would greatly benefit consumers. Researchers are investigating the potential of utilizing body heat to power wearable devices, a promising solution to the battery life issue. Therefore, self-sufficient remote health monitoring drives demand for high-performance room temperature-based sustainable and scalable thermoelectric devices.[2]

To effectively harvest the low waste heat energy in room temperature environments (<50 °C) from non-planar surfaces like the human body, the thermoelectric devices must utilize manufacturing techniques that introduce flexibility into TEG designs. Flexible thermoelectric generators (f-TEGs) can be produced through additive manufacturing techniques like

[a]Department of Mechanical Engineering, University of Maryland Baltimore County, Baltimore, MD 21250, USA. E-mail: deemadan@umbc.edu

[b]Department of Chemistry, Johns Hopkins University, Baltimore, MD 21205, USA

[c]Department of Organic and Nano Engineering, Hanyang University, Seoul 04763, Republic of Korea

[d]The Research Institute of Industrial Science, Hanyang University, Seoul 04763, Republic of Korea

[e]Advanced Research & Innovation Center, Khalifa University of Science & Technology, 127788, Abu Dhabi, United Arab Emirates

[f]Department of Aerospace Engineering, Khalifa University of Science & Technology, 127788, Abu Dhabi, United Arab Emirates

[g]Department of Chemistry and Biochemistry, University of Maryland Baltimore County, MD 21250, USA

[h]Department of Mechanical Engineering, Collage of Design and Engineering, National University of Singapore, Singapore

† Electronic supplementary information (ESI) available. See DOI: https://doi.org/10.1039/d4ta05056h

‡ These authors contributed equally to this work.

screen printing, which offer cost advantages, scalability, and manufacturing efficiency.[3,4] Bismuth telluride (Bi_2Te_3) and its different alloys have been extensively used in f-TEGs for harvesting low-waste body heat due to their high figure of merit (ZT) near 1 at room temperature.[2,5–8] This highlights its potential as a supplementary power source for wearable devices.[9,10] However, the high cost, toxicity, and rarity of tellurium raises concerns about its environmental sustainability.[11] Researchers have additionally focused on organic polymers for sustainable thermoelectric materials efforts, but a combination of a time and energy-consuming synthesis processes, TE performances below that of inorganic counterparts, and limited recyclability hinder their scalability and wide market adoption.[12–18] Therefore, research has been expanding to utilize a combination of sustainable thermoelectric materials that are naturally occurring with energy-efficient additive manufacturing methods that do not bring materials to high temperatures for long durations.[19–26]

Tetrahedrites such as $Cu_{12}Sb_4S_{13}$ (CAS) have been identified as promising sustainable thermoelectric (TE) materials. They are composed of inexpensive, earth-abundant, and non-toxic elements such as copper (Cu) and sulfur (S) and exhibit high ZTs in high-temperature applications.[27,28] Suekuni *et al.* demonstrated the first study of the thermoelectric properties of CAS using a bulk fabrication technique with a two-step annealing and ball-milling process with a ZT value of 0.7 for bulk-CAS at a temperature of 665 K.[29,30] This illustrated that CAS-based thermoelectric materials could be strong candidates under the increased phonon vibrations and lower thermal conductivities in high-temperature applications.[27–32] The decrease in phonon vibrations at lower temperatures (<600 K) contributed to a higher thermal conductivity and lower ZT of 0.15 at 340 K.[29,30] Efforts have been explored to improve the ZT of CAS at room temperature, including doping at the copper (Cu), antimony (Sb), and sulfur (S) sites. Suekuni *et al.* found that replacing Cu with Ni in $Cu_{10.5}Ni_{1.5}Sb_4S_{13}$ led to a 45% rise in ZT to 0.22 at room temperature.[29,30] However, the fabrication of bulk materials utilized in these studies involves energy and time-intensive techniques that result in rigid devices that are unsuitable for use on the human body. Therefore, while CAS shows potential as a sustainable TE material, a need exists to fabricate CAS-based composites and f-TEGs that can conform well with the human body with high performances at room temperature.

Thus, this work implements our additive manufacturing technique on CAS and its nickel and zinc-doped alloys to address historical challenges faced by printed TE composite films and f-TEGs caused by high binder weight ratios, high sintering temperature, poor interfacial connections between TE particles and the polymer binder.[33–39] The combination of a small amount of insulating chitosan binder (0.01 wt%), a wide distribution of heterogeneous (micron and nano) particle sizes, uniaxial applied mechanical pressure (20 MPa), and a low thermal budget curing process allows for the energy efficient additive manufacturing of CAS based TE composites and f-TEGs as shown in Fig. 1. The presence of nominal amounts of insulating polymer binder, nano-sized thermoelectric particles and

pores, and polymer–particle interfaces helps to decouple electrical and thermal conductivity, values usually interdependent and challenging to control independently. However, the naturally low ZT of CAS at room temperature and lower electrical conductivity values within additive manufacturing approaches highlight the need for improved room-temperature TE performances to fully leverage the advantages of the low thermal budget sustainable additive manufacturing method.

Ti_3C_2 (MXene) and graphene have been previously explored for increasing TE performances for materials such as BST with more research needed to study the effects on tetrahedrite based TE materials. MXenes, being highly conductive and serving as suitable ion hosts for effective intercalation when compared to alternatives such as graphene, were now investigated in CAS-based sustainable composites.[40–45] MXenes are a family of layered 2D transition-metal carbides and nitrides used in various applications.[46,47] They are obtained by selectively etching the "A" layers (III A or IV A elements such as Al and Si) from MAX phases, which are layered carbides or carbonitrides with a general configuration of $M_{n+1}AX_n$. MXene nanosheets improve the room temperature TE performance of CAS-based composites as they possess unique properties including high electrical conductivity, mechanical toughness, good hydrophilic nature, and the ability to bond easily with different materials.[44,45,48–51] Therefore, improved room temperature ZT was achieved for chitosan-CAS composites with the incorporation of MXene by interfacial engineering, energy barrier scattering, and nanoscale features which allowed for independent control of electrical conductivity, Seebeck coefficient, and thermal conductivity. The printed chitosan-CAS-MXene composite films and f-TEG showed a ZT 10% higher than bulk CAS at room temperature while utilizing an energy-efficient manufacturing technique with a low thermal budget as shown in Fig. 1.[27]

This work used the optimized composite TE materials and methods to fabricate a 5-couple f-TEG device using chitosan-CAS composite inks and MXene drop-casting to demonstrate the potential of low-thermal budget additive manufacturing techniques on device designs. A maximum open circuit voltage of 8.4 mV and a maximum power output of 5.3 μW was achieved with a power density of 140 μW cm^{-2} at a temperature difference (ΔT) of 25 K as shown in Fig. 1c. A flexibility test was performed by bending the TEG device at a 3.5 cm radius for 1000 cycles, resulting in an only 6% increase in internal resistance and no measurable change in voltage at a ΔT of 25 K. Additionally, a unique study was conducted to determine the impact of CAS and MXene on the environment by examining the viability of TE materials on bacterial growth. The study tested the effects of chitosan-CAS and chitosan-CAS-MXene inks on *Shewanella oneidensis* MR-1, an environmentally relevant Gram-negative bacterium, demonstrating that CAS and MXene inks are environmentally safe.[41]
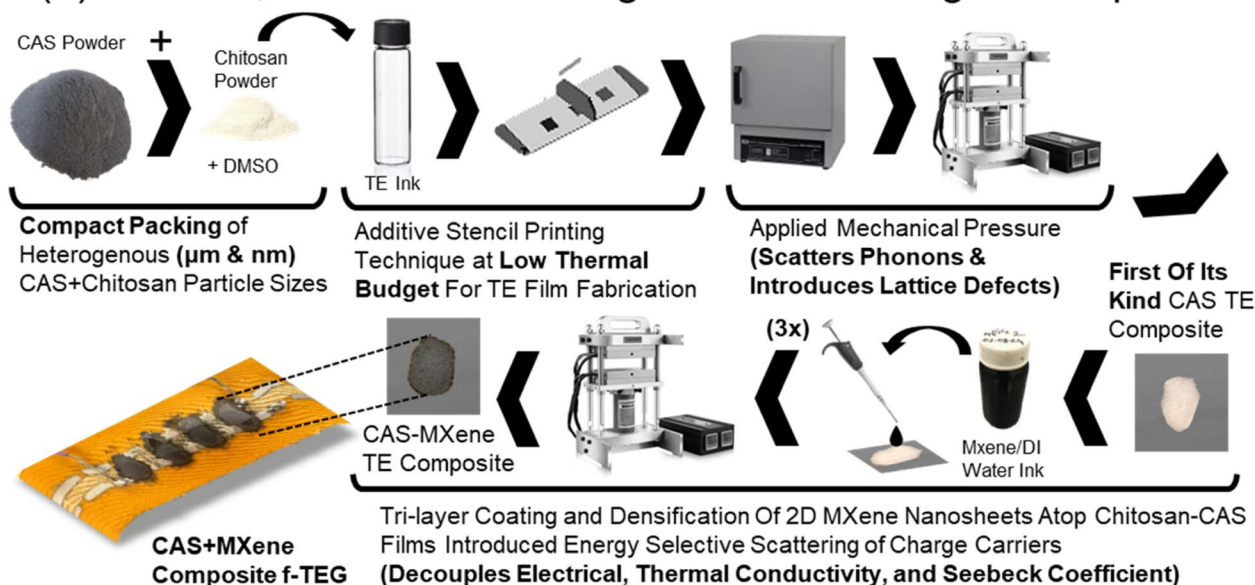
2 Results and discussion

CAS powder was utilized to fabricate chitosan-CAS and MXene based composites and f-TEGs with detailed experimental and

This journal is © The Royal Society of Chemistry 2025

J. Mater. Chem. A, 2025, **13**, 654–668 | **655**

Fig. 1 (a) Comparison of existing TEs and manufacturing techniques and their challenges, (b) graphical research flow for the fabrication of high-performance scalable and sustainable TEs composite films and f-TEGs at room temperature by investigating the impact of a low thermal budget manufacturing method including a low binder concentration, heterogeneous particle sizes, and mechanical pressure which results in (c) non-toxic CAS TE particles and MXene nanosheets to decouple electrical conductivity, Seebeck coefficient, and thermal conductivity.

material characterization procedures available in Section 3 and the ESI.† Fig. 2a shows the powder X-ray diffraction (XRD) patterns of CAS powder, and chitosan-CAS based composite films acquired and manufactured using experimental procedures detailed in the ESI.† The XRD peaks of CAS in the chitosan-CAS and chitosan-CAS-MXene composite films closely match those of the pure CAS powder and are consistent with the standard database of CAS XRD peaks (JCPDS 42-0561), indicating the presence of CAS within the composite films.[32,52,53] The low weight percentage of chitosan and MXene results in their corresponding peaks being less pronounced in the XRD analysis of composite films.

Raman analysis was conducted to confirm the presence of CAS, chitosan, and MXene peaks and investigate pressure-induced defects (Fig. 2b–e). The Raman spectra show dominant peaks corresponding to CAS (340 cm^{-1}) in chitosan-CAS films alongside peaks corresponding to MXene (236 and 690 cm^{-1}) for chitosan-CAS-MXene films (Fig. 2c and d). Additionally, a Raman peak corresponding to chitosan (1399 cm^{-1}) was present in chitosan-CAS composite films not otherwise seen in CAS powder (Fig. 2e), indicating the presence of chitosan in the composite films.[54–59] CAS and MXene Raman peak shifts were observed in the TE composite films compared to CAS powder and pristine MXene, as shown in Fig. 2c and d. Intensity changes in full-width half maximum (FWHM) indicate the introduction of dislocations and interfaces with applying pressure in composite films (Fig. 2f).[33–39,60–62] Energy-dispersive X-ray spectroscopy (EDAX) and transmission electron microscopy
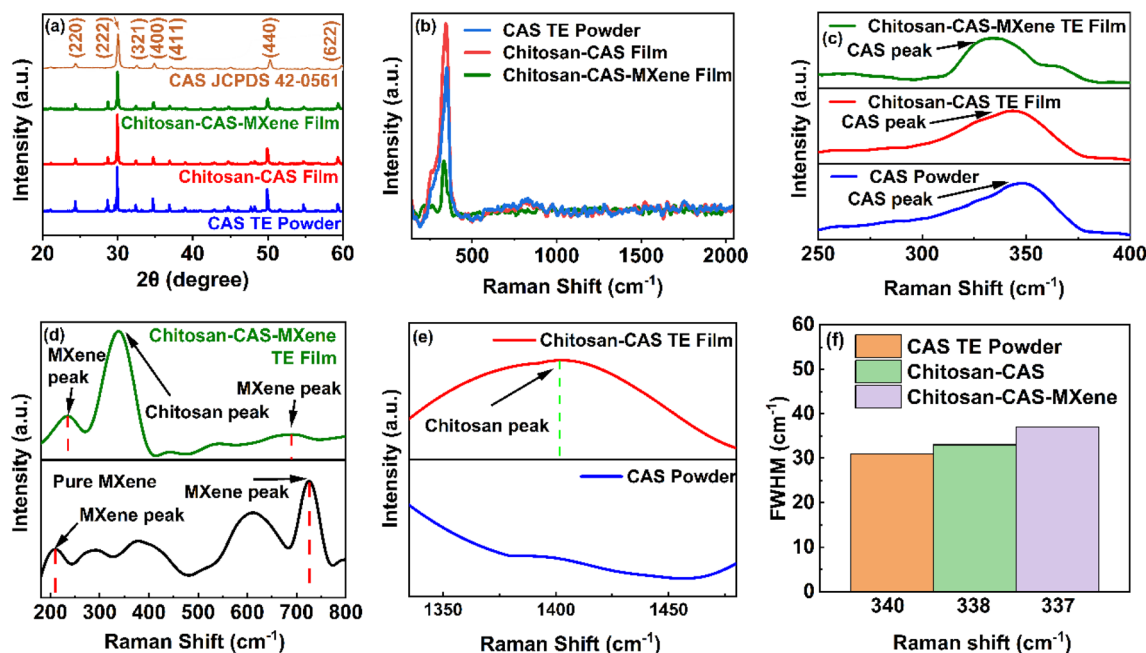
Fig. 2 (a) XRD patterns, Raman spectra of (b) CAS powder, chitosan-CAS, and chitosan-CAS-MXene TE composite film, (c) Raman spectra of CAS powder, chitosan-CAS, and chitosan-CAS-MXene TE composite film showing peaks of CAS, (d) Raman spectra of chitosan-CAS-MXene TE film and pure MXene showing peaks of MXene, (e) Raman spectra showing the chitosan peak in CAS composite films compared to CAS powder, and (f) FWHM for CAS powder, chitosan-CAS, and chitosan-CAS-MXene TE composite films.

(TEM) imaging confirm the elemental mappings of CAS powder, pristine MXene, chitosan-CAS, and chitosan-CAS-MXene composite films (Fig. S1†). Furthermore, X-ray photoelectron spectroscopy (XPS) analysis was additionally used to confirm these elemental compositions as discussed later.

The electrical conductivity, Seebeck coefficient, carrier concentration, and mobility of p-type composite films made from chitosan and tetrahedrite with different compositions $Cu_{12}Sb_4S_{13}$ (CAS), $Cu_{10}Ni_2Sb_4S_{13}$ (CNAS), and $Cu_{10}Ni_{1.5}Zn_{0.5}Sb_4S_{13}$ (CNZAS) were investigated as shown in Fig. S2.† The composite films contain tetrahedrite particles with a particle size of 325 mesh and a chitosan binder in a 1 : 10 000 ratio to the tetrahedrite particles. Fig. S2† illustrates that CAS-composite films achieved the highest average room temperature power factor of 96 $\mu W\ m^{-1}\ K^{-2}$ when compared to the doped counterparts CNAS and CNZAS, attributed to the large charge carrier concentrations when substituting Ni^{2+} with Cu^{1+} in the valence band.[27,29,30,63] The strong performance of the chitosan-CAS TE led to its selection for further experimentation in this research, representing a significant advancement in binder-based tetrahedrite composite films.

Fig. 3 demonstrates the effect of varying weight ratios of the polymer chitosan binder and the addition of MXene in the composite films on TE performances. Incorporating a polymer binder can make the additive manufacturing process for thermoelectric composites quicker and more energy-efficient than conventional bulk techniques. However, the insulative nature of the binder can significantly reduce electrical conductivity. Previous research shows that when the mass loading of an insulating polymer binder, such as epoxy, in a composite film

exceeds 15 wt%, the electrical conductivity can be as low as only 40% of the comparable bulk value. More details on polymer binder inclusions in TEGs are available in Table S1.†[33–39] Our chitosan-CAS composite film exhibits a much higher electrical conductivity, near 55% of the corresponding bulk value, without requiring a high-temperature sintering or long annealing process (Fig. 3a–c).[19–32,64–68] Table S2† compares room temperature TE performance between the present work and bulk CAS pellets.

In addition to a small amount of chitosan binder (0.01 wt%), the high electrical conductivity of the CAS composite films (comparable to bulk CAS) can be attributed to the synergetic effects of a wide distribution of heterogeneous (micron and nano) particle sizes and a uniaxial applied mechanical pressure during fabrication to replace pellet manufacturing.[27,33–39] The morphology and heterogeneous particle size distribution were investigated using a field-emission scanning electron microscope (FESEM) for chitosan-CAS and chitosan-CAS-MXene composite films (Fig. S3†). The size of TE particles was calculated using SEM images (Fig S3a and d†), and ImageJ software (Fig. S3c and f†) was estimated to be 6 μm. The CAS particles are 325 mesh, a process that filters particles in a sieve with 44 micron openings, allowing nano- and micron-sized particles to be incorporated. Due to the three-dimensional nature of the particles, such as cylinders, cones, ellipses, and prisms, a nonuniform particle size distribution is expected. The presence of microns, nanoparticles, and pores (indicated by white arrows) of the 325 mesh chitosan-CAS TE and chitosan-CAS-MXene composite film are illustrated in Fig. S3b and e.†[33–39] Additionally, cross-sectional SEM images are available in

This journal is © The Royal Society of Chemistry 2025

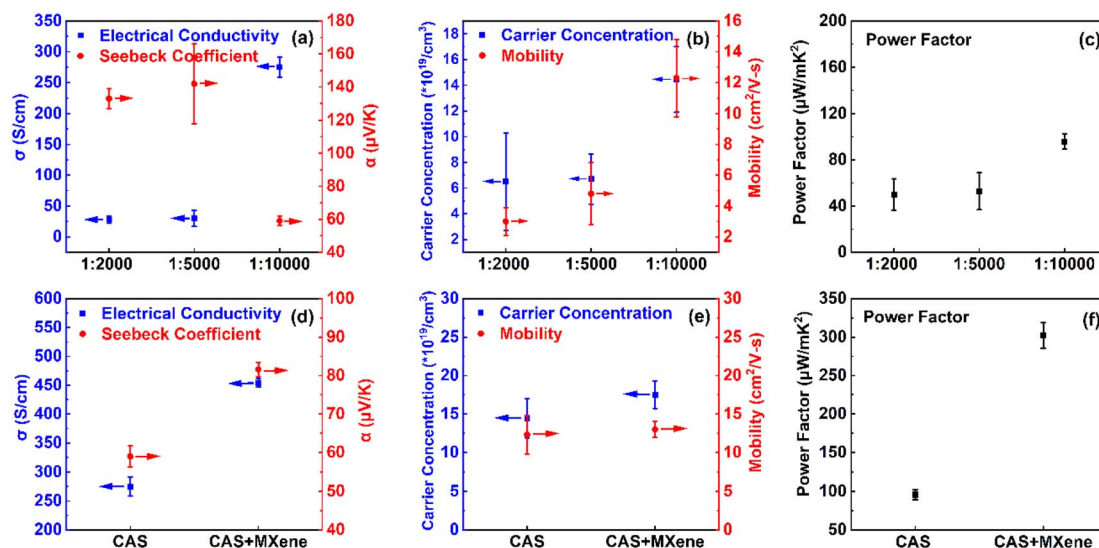*J. Mater. Chem. A*, 2025, **13**, 654–668 | **657**

Fig. 3 Room temperature (a) electrical conductivity and Seebeck coefficient, (b) carrier concentration and mobility, (c) power factor of chitosan-CAS (325 mesh) TE composite films using three different chitosan binder weight ratios (1 : 2000, 1 : 5000, and 1 : 10 000), (d) electrical conductivity and Seebeck coefficient, (e) carrier concentration and mobility, and (f) power factor of chitosan-CAS and chitosan-CAS-MXene (325 mesh, 0.01 wt%) TE composite films.

Fig. S4† clearly showing chitosan-CAS-MXene uniform distribution within the composite film.

The presence of fine (nanoscale) particles among coarse (microscale) particles in the composite film helps contribute to an increased packing density near 3.8 g cm^{-3}, approximately 88% of the bulk CAS density under the application of pressure, plastically deforming them into bigger grains with large mean free paths (detailed density measurement available in the ESI†).[33–39,69–71] These grains facilitated an enhanced charge carrier flow with minimal scattering at the grain boundary, improving the electrical conductivity of CAS composite films.[33–39]

The thermoelectric performance of chitosan-CAS composites was enhanced by 2D MXenes drop casting. The addition of 2D MXene nanosheets into chitosan-CAS films significantly improved their thermoelectric (TE) performance at room temperature.[40,47,50,51] This integration led to higher electrical conductivity and Seebeck coefficient while reducing thermal conductivity. The performance improvement is mainly determined by the quality of the synthesized MXene. High quality MXene's are produced when the MAX phase is etched using a mixed acid mixture of hydrofluoric and hydrochloric acids (HF + HCl). The X-ray diffraction (XRD) pattern of MXene (Fig. 4a) shows the disappearance of the (014) peak at 39° and the shift in the 002 peak from 9.6° to 6.19°, confirming the complete removal of Al layers and the delamination into single to few layers of MXene flakes. The formation of delaminated MXene flakes is further supported by the transmission electron microscopy image in Fig. 4b. The shift in Raman vibrations indicates that the lattice parameters of as-synthesized 2D MXenes change after etching, attributed to increased interlayer spacing, the appearance of new surface terminations, and in-plane defects.[44,45]

Upon drop-casting MXene layers onto chitosan-CAS composite films, the electrical conductivity increased by 65% and reached 454 S cm^{-1}, comparable to the bulk CAS values.[31,72] The incorporation of MXene in chitosan-CAS films increased by over 20% in carrier concentration without significantly impacting the mobility. This increase in electrical conductivity can be attributed to the synergistic characteristics of MXene, including its highly conductive metallic nature (4600 S cm^{-1}), its ability to form Ti–S elemental bonds, and its ability to facilitate the formation of chitosan-CAS/MXene hetero-interfaces causing high energy carrier injection.[41] 2D MXenes high carrier concentration contributes to its highly conductive metallic nature, which is two orders of magnitude greater than that of bulk CAS, increasing the electrical conductivity of the overall composite film.[41]

The XPS analysis was investigated for all films, as shown in Fig. 5a and S5† with full binding energy and oxidation states for the XPS peaks available in Table S3.† The XPS confirms the presence of bonding states and oxidation states of MXene and chitosan (Fig. 5b and f), as well as CAS (Fig. 5c, d and e) in chitosan-CAS-MXene films.[73–81] The formation of the Ti–S bond was observed from the newly formed Ti 2p peaks at binding energies of 455 and 463 eV in the chitosan-CAS-MXene film (Fig. 5b). Additionally, upon MXenes integration with chitosan-CAS film, the S^{2-} peaks broaden in the S 2p spectrum, further confirming the formation of Ti–S bonds and increasing the electrical conductivity of chitosan-CAS-MXene composite films (Fig. S5a, c and f†).[82–84] The formation of Ti–S bonds has been demonstrated to effectively increase the charge carrier concentration and electrical conductivity due to the bonding defects induced by sulfur in the chitosan-CAS-MXene film.[80,81]

Ultraviolet photoelectron spectroscopy (UPS) and ultraviolet-visible (UV-vis) spectroscopy were used to determine the work
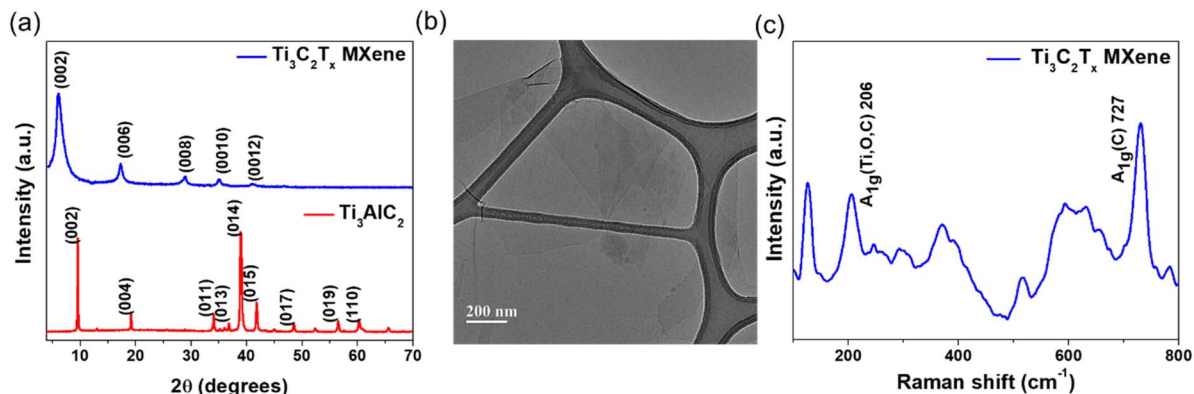
658 | J. Mater. Chem. A, 2025, 13, 654–668

This journal is © The Royal Society of Chemistry 2025

Fig. 4 Characterization of as-synthesized MXenes. (a) XRD pattern of MXenes showing the delaminated nanosheets, (b) TEM image confirming the presence of single to few layers of MXenes, (c) Raman spectra of 2D MXene nanosheets showing MXene vibrations.

function (ϕ), energy gap (E_g), valence band maximum (E_V) with reference to Fermi level (E_F), and electron affinity (χ) for CAS powder, 2D MXene nanosheets, chitosan-CAS and chitosan-CAS-MXene composite films (Fig. 6 and S6†). The energy band scheme for MXene and chitosan-CAS (before contact) and chitosan-CAS-MXene film (post contact) were constructed using these ϕ, E_g, E_V, E_F, and χ values (Fig. 6j). MXenes introduction in the chitosan-CAS film resulted in the formation of a chitosan-CAS/MXene interface with two distinct work functions ($\phi_{\text{chito-san-CAS}} = 4.38$ eV, $\phi_{\text{MXene}} = 4.30$ eV) (Fig. 6k). The Fermi levels of chitosan-CAS and MXene align at equilibrium, resulting in a distinct work function for the chitosan-CAS-MXene film ($\phi_{\text{chitosan-CAS-MXene}} = 4.37$ eV). This alignment occurs through downward conduction and valence band bending on the chitosan-CAS film, as is consistent when $\phi_{\text{p-type semiconductor}} >$

ϕ_{metal}, leading to the formation of an interface potential ($V_B = \phi_{\text{chitosan-CAS}} - \phi_{\text{MXene}}$) of 0.08 eV at the chitosan-CAS/MXene interface.[27,46,47,51,85]

Previous research has shown that low energy charge carriers are scattered within modest interface potentials (0.05–0.1 eV) contribute to improvements in Seebeck coefficient while allowing for the unobstructed injection of high energy carriers into the composite film contributing to improvements in electrical conductivity, a concept known as energy barrier scattering.[85,86] With the V_B of the chitosan-CAS-MXene film, MXene injects high-energy charge carriers into the chitosan-CAS film, thereby increasing the electrical conductivity of the composite film by 60%, reaching a value of 454 S cm^{-1}. Moreover, the low-energy carriers are back-scattered due to the V_B, resulting in a Seebeck coefficient of 82 μV K^{-1} for the chitosan-CAS-MXene
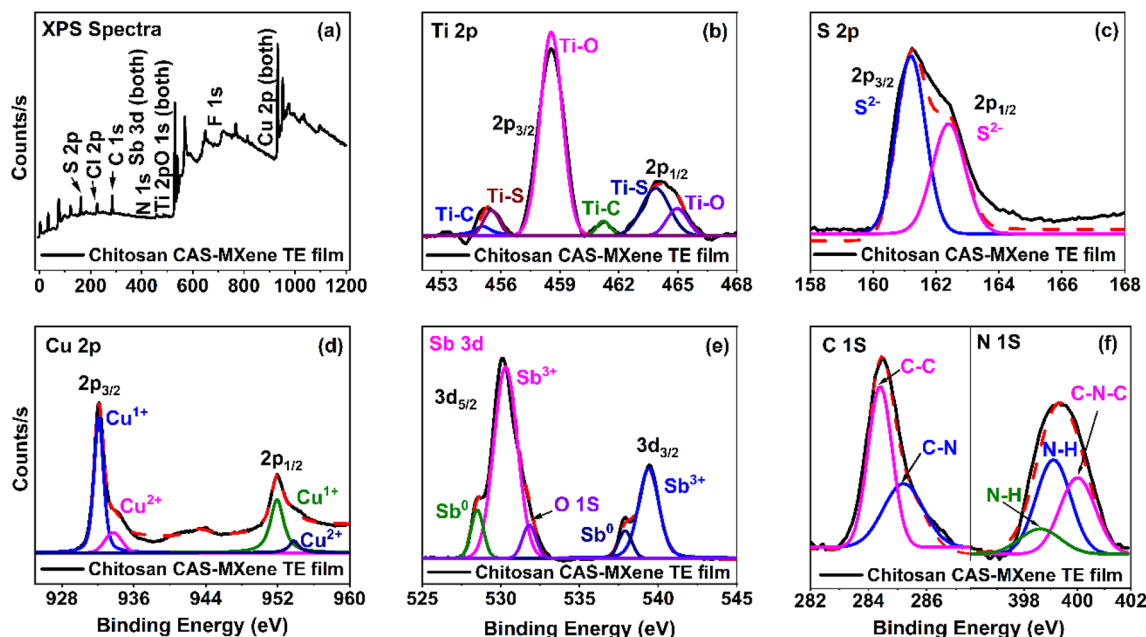

Fig. 5 (a) Full survey spectra of chitosan-CAS-MXene TE composite film, high-resolution XPS spectra of (b) Ti 2p, (c) S 2p, (d) Cu 2p, (e) Sb 3d, (f) C 1s left, N 1s right for chitosan-CAS-MXene film.
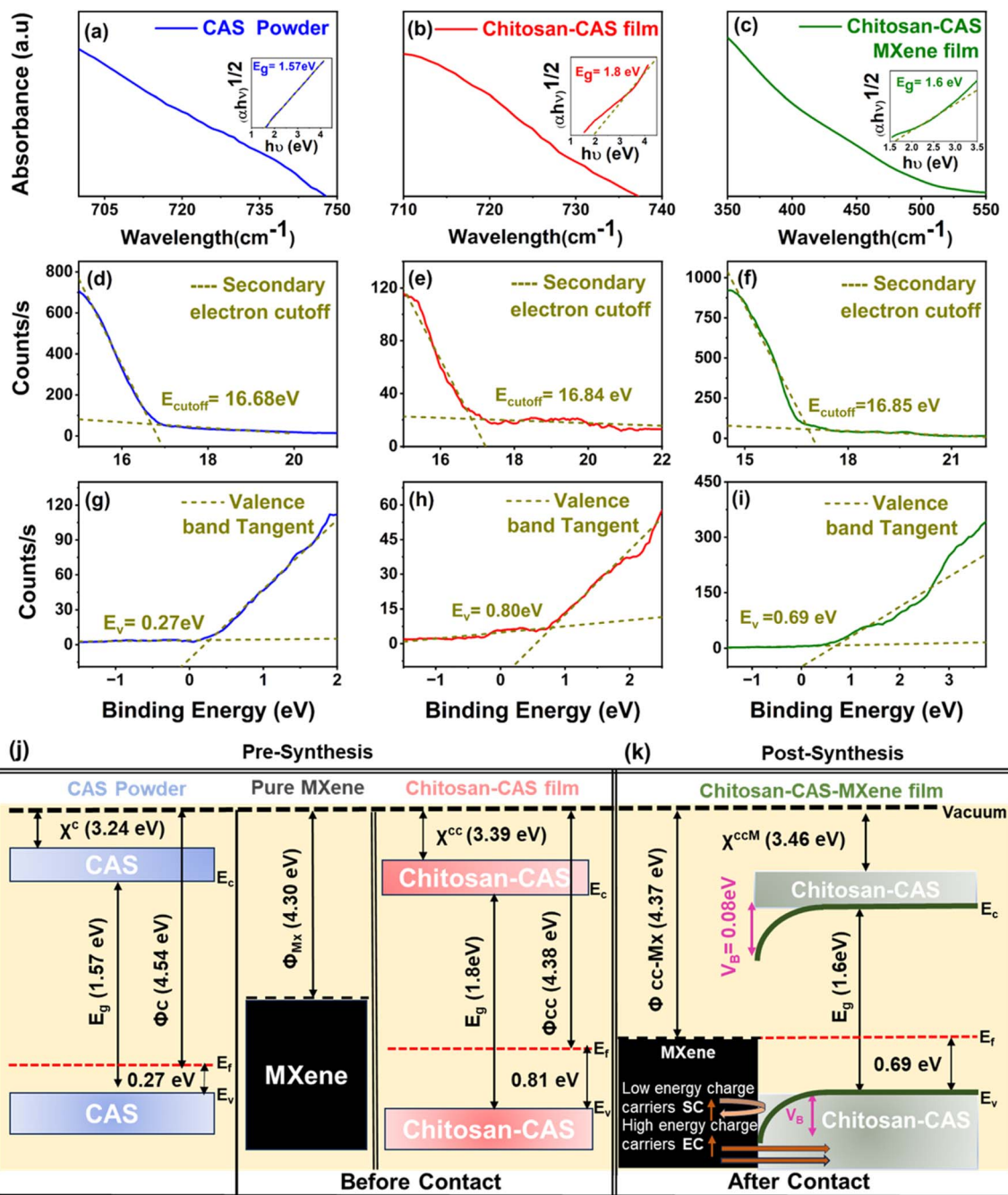
Fig. 6 UPS spectra of (a) CAS powder, (d) chitosan-CAS, and (g) chitosan-CAS-MXene TE composite film at the secondary edge region for direct determination of the work function. UPS spectra of (b) CAS powder, (e) chitosan-CAS, and (h) chitosan-CAS-MXene TE composite film at the valence band edge region to measure the valence band maximum. UV-Vis-NIR absorption spectra and Tauc plots (insets) of (c) CAS powder, (f) chitosan-CAS, and (i) chitosan-CAS-MXene TE composite film to determine the bandgap. Energy scheme (j) before and (k) after metallic MXene and p-type CAS contact/synthesis.

composite film, a 40% improvement compared to the Seebeck coefficient of chitosan-CAS film without MXene (Fig. 3d). Therefore, adding MXene onto chitosan-CAS composite films resulted in energy barrier scattering, contributing to the decoupling and increase in the electrical conductivity and Seebeck coefficient.[41,86]

The introduction of energy barrier scattering by MXene resulted in a threefold increase in the power factor of chitosan-

CAS composites, resulting in a power factor of 302 $\mu W\ m^{-1}\ K^{-2}$ (as shown in Fig. 3f). Notably, this high-power factor of the chitosan-CAS-MXene composite film, 5% higher than bulk CAS values, is achieved at room temperature without requiring a high-temperature and lengthy fabrication process.[27]

The measured room temperature in-plane and out-of-plane thermal conductivity of chitosan-CAS films were 0.70 W m^{-1} K^{-1} and 0.71 W m^{-1} K^{-1}, respectively. The thermal conductivity

660 | J. Mater. Chem. A, 2025, 13, 654–668

This journal is © The Royal Society of Chemistry 2025

of composite films was measured using the 3ω method to provide reliable thermal conductivity of films, following our reported sample preparations and the analysis of the AC-modulated thermal response.[25,26] The in-plane and out-of-plane thermal conductivity were similar, meaning the composite film exhibited polycrystalline and isotropic behavior indicated through the randomly dotted bright SAED pattern rings shown in Fig. 7f and i not otherwise seen in CAS powder Fig. 7c. More details on the 3ω testing methodology is available in the ESI.† [33–39,82,87] The measured thermal conductivity of the chitosan-CAS film is 55% of the bulk CAS value, driven by the presence of nanoscale features (nanoparticles and nanopores).[27,28] These nanoscale features coupled with pressure-induced lattice defects, the insulating chitosan binder, and polymer–particle interfaces scatter phonons within the composite film and decrease thermal conductivity.

Dresselhaus *et al.* pioneered nanostructuring by demonstrating how nanoscale features can scatter phonons while allowing for an unobstructed flow of charge carriers.[86,88,89] Experiments conducted by Lim *et al.* report optimal reductions in thermal conductivity for bulk CAS are achieved when the particle size is near 25 nm.[88] These studies suggest that nanoscale features can help decouple thermal and electrical conductivity, improving overall TE performance. These nanoscale features in the chitosan-CAS composite film were proven by FESEM and Brunauer–Emmett–Teller (BET) analysis (Fig. S7a–f†). The average particle and pore size for the CAS composite films was estimated to be ~10 nm (for ~24 000 particles) and ~2 nm (for ~71 000 pores in a 3.27 μm × 2.45 μm area), respectively, through ImageJ software shown in Fig. S7a and b.† The presence of nanopores (0.00017 cm³ in 1 gram) was proven by BET analysis (Fig. S7c and d†). Additionally, the N₂
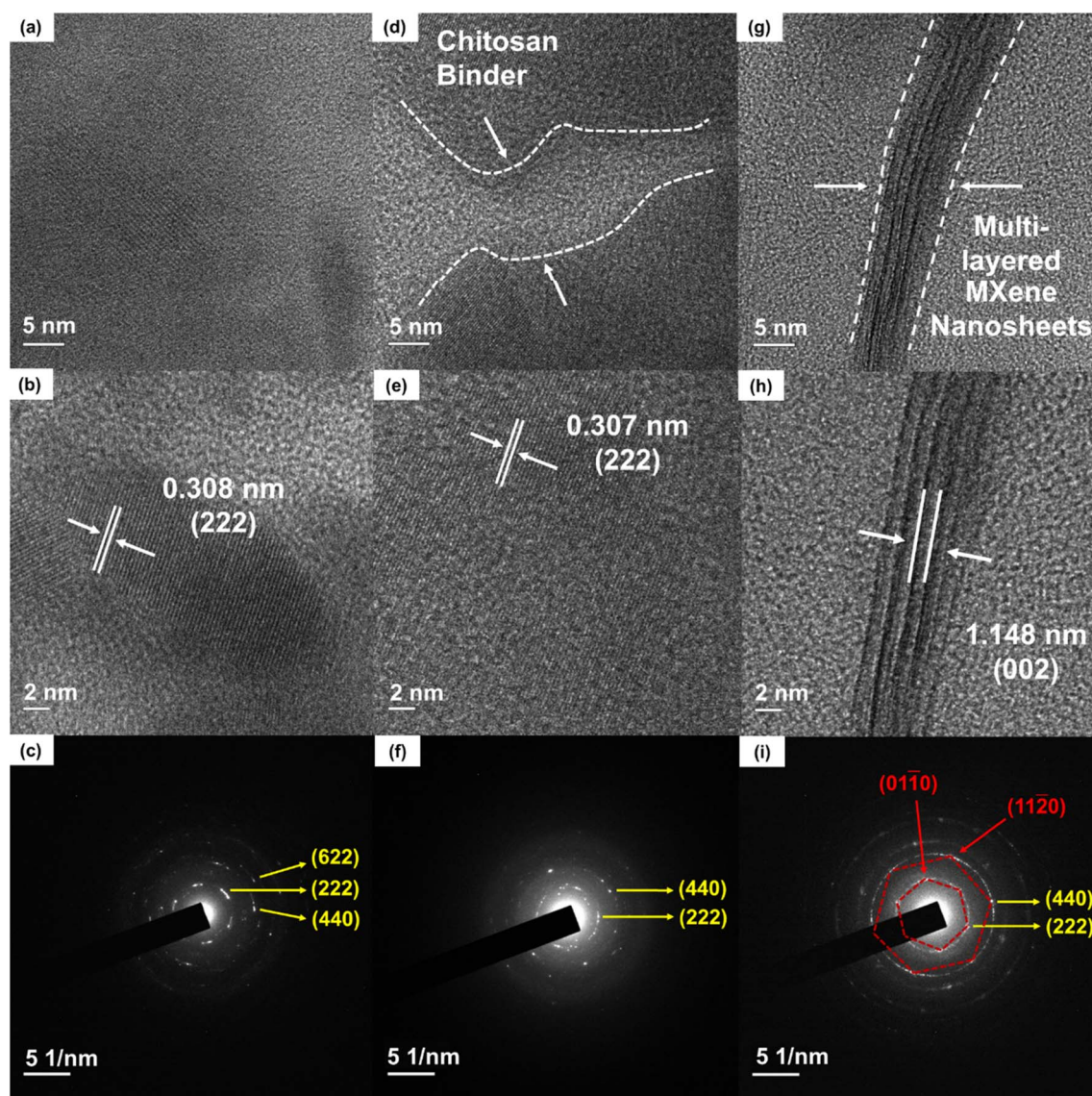

Fig. 7 HRTEM images of (a and b) CAS powder, (d and e) chitosan-CAS TE composite film showing the presence of chitosan-CAS interfaces, (g and h) chitosan-CAS-MXene TE composite film showing the presence of MXene-CAS interfaces at different magnifications. SAED pattern of (c) CAS powder, (f) chitosan-CAS TE composite film, and (i) chitosan-CAS-MXene TE composite film.

adsorption–desorption isotherm curve (Fig. S7c and d†) shows typical type IV isotherm corresponding to a mesoporous material (pore diameter between 2 and 50 nm), confirming the presence of nanoscale pores.[57,86,89,90] Furthermore, uniaxial pressure on the composite film is believed to introduce lattice defects, which scatter phonons and reduce thermal conductivity.[86,89,91] This was confirmed through Raman and HRTEM analyses of CAS powder and chitosan-CAS composite films (Fig. 7a and d). The Raman peak shifts (Fig. 2c and e) and intensity changes in FWHM (Fig. 2f) indicate the presence of lattice defects changing density of states (DOS) effective mass and weighted mobility.[7,8,33–39,86,89,91] The DOS effective mass and weighted mobility of the chitosan-CAS film were calculated using Synder's equation to be 1.4 m_e and 20 cm^2 V^{-1} s^{-1}, respectively, representing a 35% and 30% change from the bulk values of 1.85 m_e and 28 cm^2 V^{-1} s^{-1}.[9,33–39] These changes in DOS and weighted mobility due to applied pressure also indicate increased phonon vibrations contributing to the decreases observed in thermal conductivity. Furthermore, XPS analysis shows peak shifts from bulk CAS to chitosan-CAS and chitosan-CAS MXene films, confirming the introduction of lattice defects under applied mechanical pressure (Fig. 5a–c and S5†).[92–94] The introduction of these pressure-induced defects resulted in lattice spacing changes, as seen in HRTEM Fig. 7b and e.[28,72,95–97]

Adding 2D MXene nanosheets to the chitosan-CAS composite film decreased thermal conductivity. The resulting chitosan-CAS-MXene film exhibited a thermal conductivity of 0.41 W m^{-1} K^{-1} at room temperature, a 41% decrease compared to the chitosan-CAS film. This change in thermal conductivity with the inclusion of the 2D MXene nanosheet is hypothesized to the similar characteristics seen in the chitosan-CAS film, including increases in the number of nanoscale features, further pressure-induced lattice defects, and the formation of a MXene/CAS interface.

Fig. S7† (FESEM and BET analysis) shows an increase in the nanoscale features in chitosan-CAS-MXene film compared to the chitosan-CAS film. The number of nanoparticles rose to ~41 000, and the number of nanopores rose to ~75 000, as shown in Fig. S7e–h† vs. the chitosan-CAS FESEM image Fig. S7a–d† in the same size image area. The average particle and pore size for the chitosan-CAS-MXene composite films was estimated to be ~9 nm and ~3 nm, respectively, through ImageJ software shown in Fig. S7e and f.† The N_2 adsorption–desorption isotherm curve (Fig. S7h†) confirmed the presence of nanoscale pores.[91,98,99] The presence of nanopores increased tenfold to 0.00110 cm^3 in 1 gram, as shown by BET analysis (Fig. S7g†) as compared to the chitosan-CAS film BET (Fig. S7c†). The increase in nanoscale features with the addition of MXene caused an increase in phonon scattering, contributing to decreased thermal conductivity in the chitosan-CAS-MXene film.

Further pressure lattice defects were introduced upon adding the MXene layer in the chitosan-CAS-MXene film scatter phonons, which decreased overall thermal conductivity.[86,89,91] Raman peak shifts and FWHM intensity changes demonstrate the increased lattice defects found in chitosan-CAS-MXene films (Fig. 2c, d and f). Similarly, XPS analysis Fig. 5 shows the Sb
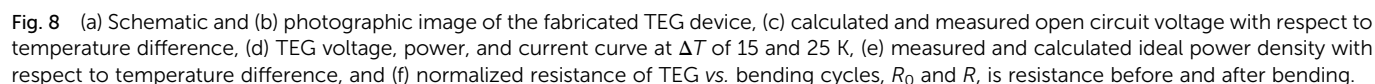
peak broadening and a downward shift in the N 1s peak, indicating increased phonon vibrations due to additional applied pressure.[86,92–94] Moreover, introducing these defects by applying pressure resulted in lattice spacing changes seen in HRTEM Fig. 7e and h.[28,33–39,95–97] These defects were shown to cause changes in the calculated DOS effective mass, increasing 65% to 2.35 m_e and weighted mobility doubling to 47 cm^2 V^{-1} s^{-1}. These changes in DOS effective mass and weighted mobility further enhance the phonon scattering that decreases the thermal conductivity of chitosan-CAS-MXene films. The addition of MXene formed an interface with CAS as shown in the chitosan-CAS-MXene HRTEM images Fig. 7g and h, not otherwise present in the chitosan-CAS HRTEM image Fig. 7d. This interface also facilitated phonon scattering, further decreasing the thermal conductivity.[33–40,100–102]

Finally, the chitosan-CAS-MXene composite film demonstrated an increased electrical conductivity and Seebeck coefficient while simultaneously facilitating a decrease in thermal conductivity at room temperature with a ZT of 0.22, a four and a half fold increase compared to chitosan-CAS composite films. This confirms MXene's decoupling of thermoelectric parameters in CAS based TE composites, achieving a ZT 10% higher than bulk CAS while utilizing an energy-efficient additive manufacturing technique. This 450% increase in room temperature ZT outperforms the up to ~50% increases previously seen by other researchers with the addition of graphene and MXene nanosheets onto conventional chalcogenide TE materials.[46,47]

To demonstrate the flexibility and scalability of CAS and MXene based f-TEG, a 5 single-leg CAS TEG device (5 cm × 2 cm × 250 μm) (length × width × height) was fabricated by stencil printing with a resistance of 3.3 ohms (Fig. 8a and b). The voltage and power output characterizations were performed at room temperature, with more detailed setup information shown in Fig. S8.† The measured voltage output increased linearly with ΔT. It was comparable to the calculated open-circuit voltage using the Seebeck coefficient of chitosan-CAS-MXene films (Fig. 8c). The maximum power output of 5.3 μW was achieved at a ΔT of 25 K with a closed-circuit voltage of 4.2 mV and a current of 1.3 mA (Fig. 8d). The maximum power density of 140 μW cm^{-2} (including spacing between thermoelements) was achieved at ΔT of 25 K. The increasing difference between the measured and calculated power density curves with ΔT can be attributed to the increased device resistance at higher temperatures (Fig. 8e). Table S4† compares the existing literature on TEG device manufacturing (ESI†).

A flexibility test was conducted to assess the device's real-world durability, measuring its resistance and voltage output during bending, serving as an indicator for potential cracking.[33–39] This flexibility test involved 1000 cycles of bending the device at a radius of 3.0 cm. Fig. 8f and S8f† illustrates the device's consistent resistance and voltage output throughout the test. The device's internal resistance increased by 6% after bending, and its voltage output decreased by 2%, demonstrating flexibility with no significant cracking.

The potential environmental sustainability impact of chitosan-CAS and chitosan-CAS-MXene thermoelectric materials was tested through a Shewanella oneidensis MR-1 bacterial

662 | J. Mater. Chem. A, 2025, 13, 654–668

This journal is © The Royal Society of Chemistry 2025

Fig. 8 (a) Schematic and (b) photographic image of the fabricated TEG device, (c) calculated and measured open circuit voltage with respect to temperature difference, (d) TEG voltage, power, and current curve at ΔT of 15 and 25 K, (e) measured and calculated ideal power density with respect to temperature difference, and (f) normalized resistance of TEG vs. bending cycles, R_0 and R, is resistance before and after bending.

viability test (Fig. S9†). The test followed a previously reported protocol for the growth-based viability (GBV) assay on *Shewanella oneidensis* MR-1, a Gram-negative bacterium, with three biological replicates. Viability, a measure of bacterial concentration, indicates bacterial cell growth when exposed to materials at specific concentrations.[103–105] Fig. S9† presents the normalized viability results of both chitosan-CAS and chitosan-CAS-MXene TE materials in water, with concentrations up to 600 mg l^{-1}, on *Shewanella oneidensis* MR-1. Viability near 1 across all tested concentrations suggests that strong bacterial growth and the materials are environmentally safe should these thermoelectric devices degrade, leak, or be exposed to the natural aqueous environment post-use to bacteria within that concentration range. Therefore, chitosan-CAS and chitosan-CAS-MXene inks are considered environmentally safe up to 600 mg l^{-1} exposure concentrations.

The low thermal budget manufacturing method, earth abundance, environmental safety, and nontoxicity combination demonstrate the sustainability of the methods and materials used to manufacture high-performance chitosan-CAS-MXene composites and f-TEGs for low-waste heat applications. Similarly, the additive manufacturing technique facilitates the cost-effective scalability of these f-TEGs. For the first time, this study demonstrates the ability of CAS to effectively transform low-waste heat energy into useable energy by combining a chitosan-CAS composite-based TE material coupled with 2D MXene nanosheets within f-TEG devices. Therefore, naturally available tetrahedrites present unique advantages, allowing for the widespread adoption of safe TEG in wearable and health monitoring devices. The f-TEG 5.3 μW power output at a ΔT of 25 K closely matches the average power requirements of wearable monitoring

sensors and devices. In future work, we aim to utilize the scalability of our low-cost and energy-efficient manufacturing technique to print and connect more TE legs in series, demonstrating tetrahedrite's potential to harness low-waste body heat as a self-sufficient power source for wearable monitoring devices.

3 Experimental section

3.1 Materials

The materials used in this research include pure 325 mesh $Cu_{12}Sb_4S_{13}$ (CAS) powder and two compound derivatives obtained by substituting the Cu site with Ni ($Cu_{10}Ni_2Sb_4S_{13}$, CNAS) and Ni and Zn ($Cu_{10}Ni_{1.5}Zn_{0.5}Sb_4S_{13}$, CNZAS). The three powder compounds were purchased from Wuhan Dongxin Inc., China. Chitosan powder (MP Biomedicals, LLC), dimethyl sulfoxide (DMSO, ≥99.7%, extra dry, ACROS Organics), salicylic acid, and Luria–Bertani (LB) broth and agar were purchased from Fisher Scientific. Ti_3AlC_2 MAX-phase powders (particle size <200 μm, Ukraine) were obtained from Carbon-Ukraine Ltd. The 5 mm thick non-adhesive Kapton substrate was purchased from Tape-Case, IL, US. HEPES, NaCl, phosphate buffer saline (PBS) powders, 35% hydrochloric acid (HCl) solution, and 99.995% lithium fluoride (LiF) powder were purchased from Sigma Aldrich. *Shewanella oneidensis* MR-1 106686 was purchased from ATCC. Kanamycin was purchased from GoldBio. Millipore deionized water (DIW) was used without further treatment. All chemicals were used as received without any further purification.

3.2 Synthesis of chitosan-tetrahedrite TE composite ink

The TE composite ink was synthesized by combining a chitosan binder solution with active TE tetrahedrite particles. The

This journal is © The Royal Society of Chemistry 2025

J. Mater. Chem. A, 2025, **13**, 654–668 | **663**

chitosan binder solution was synthesized by mixing chitosan powder, DMSO, and salicylic acid at 60 °C for 24 hours. The binder-to-particle weight ratio was optimized by combining the chitosan binder with pure tetrahedrite TE active particles at various weight ratios (1 : 2,000, 1 : 5,000, and 1 : 10 000). The binder-to-particle weight ratio of 1 : 10 000 had the highest power factor and was chosen for the remainder of the experimental work, as shown in Fig. 3c. Different tetrahedrite TE particle compounds (CAS, CNAS, and CNZAS) were combined with the chitosan binder at the optimized ratio. To ensure the homogeneous dispersion of active TE particles in the chitosan binder, the inks were mixed in a vortex mixer for 2 minutes, followed by sonication for 30 minutes. Before the ink deposition on a substrate, the ink was re-mixed in a vortex mixer for 15 seconds.

3.3 Fabrication of chitosan-CAS composite films

The chitosan-CAS TE composite films were fabricated using a stencil printing technique. This was done by administering the TE composite ink on a Kapton substrate using a custom-designed printing mask. The printing mask was prepared by stacking several layers of single-side tape (Business Source®) together to achieve a film thickness of 250–300 μm. This was followed by curing the printed composite films at 120 °C for 10 minutes. The dried films were then pressed at 20 MPa for 30 minutes using a hydraulic press. Kapton was used as a substrate due to its poor adhesive quality, ensuring films had a free-standing structure, which aided in precise thickness measurements post-pressing.

3.4 Synthesis of $Ti_3C_2T_x$-MXene

The MXenes were synthesized following the protocols for etching the Al-rich Ti_3AlC_2 MAX phase.[45,106] Briefly, 2 g of Ti_3AlC_2 MAX phase was selectively etched by slowly adding Al-rich Ti_3AlC_2 to a solution containing HF (12 M) and HCl (15 M) in a polyethylene terephthalate plastic bottle over a period of approximately 5 minutes due to the exothermic nature of the reaction. The mixture was stirred at 300 rpm with a polytetra-fluoroethylene-coated stir bar at 35 °C for 24 h. The reaction mixture was washed multiple times with deionized water *via* centrifugation at 3500 rpm until the pH reached 7. The multi-layered MXenes were further delaminated in a 5 wt% lithium chloride solution. The stable suspension of monolayered MXenes was obtained by centrifuging delaminated MXene at 3500 rpm for 5 minutes to obtain a clear supernatant. This supernatant was further centrifuged at 10 000 rpm for 2 h to concentrate the solution. The concentrated MXene nanosheets were finally dispersed in a Millipore water solution to obtain a stable colloidal suspension with concentrations as high as 75 mg ml^{-1}.

3.5 Fabrication of chitosan-CAS-MXene composite films

As-manufactured chitosan-CAS films were drop casted with 75 μl of a MXene and DIW solution with a 75 mg ml^{-1} concentration films to form an MXene layer that completely coated the top of the films surface. The MXene layer and the CAS-chitosan

composite film were then cured at 70 °C for 20 minutes in the oven. The applied MXene layer and the CAS-chitosan composite film were pressed at 20 MPa for 20 minutes to enhance the bonding between the MXene layers and the CAS-chitosan composite film. This process was repeated until 3 layers of MXene were formed, ensuring a uniform coating to form the final chitosan-CAS-MXene composite film.

3.6 Fabrication of chitosan-CAS-MXene composite f-TEG devices

The TEG device was fabricated on a flexible Kevlar substrate with a gold-coated Cu electrode (purchased from South Korea PASF250, Sueco Advanced Material Co., Ltd). Before printing, a commercially available solder paste was coated on the gold electrodes to improve the electrical and mechanical connections between TE elements and electrodes.[33,34,39] Then, CAS composite inks were stencil printed on the substrate using the custom-designed printing mask. The same type of tape mask (Business Source®) was used to help print the desired dimension of the thermoelements. The pattern on the mask was manufactured by a laser cutter with dimensions of (2 mm × 6 mm) (width × length) for each thermoelement. Then, the device was cured at 120 °C for 10 min, hot pressed at 160 °C, and 20 MPa for 30 min. Each thermoelement measured approximately 3 mm × 7 mm × 275 μm (width × length × thickness). A MXene and distilled water solution with a 75 mg ml^{-1} concentration were dropped on top of the CAS-chitosan composite thermoelements to form an MXene layer. The MXene layer and the CAS-chitosan composite film were then cured at 70 °C for 20 minutes in the oven. The applied MXene layer and the CAS-chitosan composite film were pressed at 20 MPa for 20 minutes to enhance the bonding between the MXene layers and the CAS-chitosan composite thermoelements. This process was repeated until 3 layers of MXene were formed, ensuring a uniform coating to form the final chitosan-CAS-MXene composite device.

4 Conclusion

In summary, this work developed a scalable and sustainable CAS-based f-TEG with high performance at room temperature. Chitosan-CAS composite films were fabricated using a small amount of binder (0.01 wt%), a heterogeneous micron and nano-sized particle distribution, and applied pressure (20 MPa) using a low thermal budget additive manufacturing approach. 2D nanosheets of MXene, a newly discovered nanoparticle transition metal carbide, were drop-casted onto chitosan-CAS composite films to improve their room temperature TE performance further. The electrical conductivity, Seebeck coefficient, and thermal conductivities of our chitosan-CAS-MXene films and f-TEGs were decoupled using a combination of interfacial engineering, energy barrier scattering, and nanoscale features. MXenes were able to effectively decouple all thermoelectric properties by (1) a naturally high electrical conductivity, (2) the formation of an energy barrier at the CAS/MXene interface introducing an energy-dependent scattering of charge carriers, decoupling the electrical conductivity and Seebeck coefficient,

664 | *J. Mater. Chem. A*, 2025, **13**, 654–668

This journal is © The Royal Society of Chemistry 2025

and (3) the increase in nanoscale features scattering phonons while allowing for the unobstructed flow of electrons, decoupling the electrical and thermal conductivities. The inclusion of MXene into chitosan-CAS composite TE films resulted in a high ZT of 0.22 at room temperature, a first for a CAS-based printed TE composite film being 10% higher than bulk CAS. The achieved power output of 5.3 μW and power density of 140 μW cm^{-2} at a temperature difference of 25 K for a 5-leg chitosan-CAS-MXene device serves as a novel advancement in sustainably manufactured TEG devices. Furthermore, a flexibility test showed that the fabricated TEG device could conform well to non-planar surfaces, demonstrating its real-world capability to capture the low-waste heat energy of the human body efficiently. The scalability found within the printing additive manufacturing method allows for fabricating numerous thermoelements in series for f-TEG devices without making large changes in the manufacturing infrastructure while simultaneously improving the voltage and power output to match the demands of wearable sensors. Lastly, a first-of-its-kind bacterial viability test on thermoelectric materials demonstrated the environmental safety of chitosan-CAS and chitosan-CAS-MXene inks, paving the way for their environmentally friendly use. This achievement represents the first successful creation of a high-performance room temperature f-TEG for low-waste heat applications. This demonstrates the combination of scalable and environmentally sustainable materials and methods is an effective strategy for the fabrication of chitosan-CAS-MXene based f-TEGs that can potentially harvest the low waste heat energy from the human body.

Data availability

The data supporting this article have been included as part of the ESI.†

Author contributions

Priyanshu Banerjee designed the experiments, analyses and drafted the manuscript. Jiyuan Huang performed all the experimental work and analyzed the results. Jacob Lombardo analyzed the results, edited, and finalized the manuscript, Swapnil B. Ambade provided the MXene material, Rohan B. Ambade supervised and performed all the characterizations. Tae Hee Han supervised all the surface characterizations. Srushti Kulkarni analyzed the results and edited the manuscript, Shreyasi Sengupta conducted sustainability test, Zeev Rosenzweig supervised sustainability test. Sichao Li conducted the thermal conductivity measurements. Sunmi Shin designed and supervised the thermal conductivity measurements, Deepa Madan supervised, designed, and edited the whole research. All the authors discussed the results and commented on the manuscript.

Conflicts of interest

The authors declare that they have no known competing financial interests or personal relationships that could have appeared to influence the work reported in this paper.

Acknowledgements

References

1 X. Gong, K. Huang, Y. H. Wu and X. S. Zhang, *Sens. Actuators, A*, 2022, **345**, 113821, DOI: **10.1016/j.sna.2022.113821**.

2 A. Nozariasbmarz, H. Collins, K. Dsouza, M. H. Polash, M. Hosseini, M. Hyland, J. Liu, A. Malhotra, F. M. Ortiz, F. Mohaddes, V. P. Ramesh, Y. Sargolzaeiaval, N. Snouwaert, M. C. Özturk and D. Vashaee, *Appl. Energy*, 2020, **258**, 114069, DOI: **10.1016/j.apenergy.2019.114069**.

3 S. Mortazavinatanzi, A. Rezaniakolaei and L. Rosendahl, *Sensors*, 2018, **18**, 989, DOI: **10.3390/s18040989**.

4 S. J. Kim, J. H. We and B. J. Cho, *Energy Environ. Sci.*, 2014, **7**, 1959, DOI: **10.1039/c4ee00242c**.

5 V. Shalini, S. Harish, J. Archana, H. Ikeda and M. Navaneethan, *J. Alloys Compd.*, 2021, **868**, 158905, DOI: **10.1016/j.jallcom.2021.158905**.

6 Z. Soleimani, S. Zoras, B. Ceranic, Y. Cui and S. Shahzad, *Nano Energy*, 2021, **89**, 106325, DOI: **10.1016/j.nanoen.2021.106325**.

7 R. M. Siddique, S. Mahmud and B. Van Heyst, *Renewable Sustainable Energy Rev.*, 2017, **73**, 730, DOI: **10.1016/j.rser.2017.01.177**.

8 B. Poudel, Q. Hao, Y. Ma, Y. Lan, A. Minnich, B. Yu, X. Yan, D. Wang, A. Muto, D. Vashaee, X. Chen, J. Liu, M. S. Dresselhaus, G. Chen and Z. Ren, *Science*, 1979, **320**, 634, DOI: **10.1126/science.1156446**.

9 M. Hyland, H. Hunter, J. Liu, E. Veety and D. Vashaee, *Appl. Energy*, 2016, **182**, 518, DOI: **10.1016/j.apenergy.2016.08.150**.

This journal is © The Royal Society of Chemistry 2025

J. Mater. Chem. A, 2025, **13**, 654–668 | **665**

10 A. Nozariasbmarz, F. Suarez, J. Houston Dycus, M. J. Cabral, J. M. LeBeau, M. C. Oztürk and D. Vashaee, *Nano Energy*, 2020, **67**, 104265, DOI: 10.1016/j.nanoen.2019.104265.

11 Y. Shi, C. Sturm and H. Kleinke, *J. Solid State Chem.*, 2019, **270**, 273, DOI: 10.1016/j.jssc.2018.10.049.

12 O. Bubnova, Z. U. Khan, A. Malti, S. Braun, M. Fahlman, M. Berggren and X. Crispin, *Nat. Mater.*, 2011, **10**, 429, DOI: 10.1038/nmat3012.

13 J. Huang, H. Li, E. Kirksey, C. Hoffman, H. Jang, J. Wagner, D. Madan and H. E. Katz, *J. Appl. Phys.*, 2019, **125**, 125502, DOI: 10.1063/1.5089872.

14 T. Mukhopadhyaya, J. Wagner, T. D. Lee, C. Ganley, S. Tanwar, P. Raj, L. Li, Y. Song, S. J. Melvin, Y. Ji, P. Clancy, I. Barman, S. Thon, R. S. Klausen and H. E. Katz, *Adv. Funct. Mater.*, 2024, **34**, 2309646, DOI: 10.1002/adfm.202309646.

15 Y. Sun, P. Sheng, C. Di, F. Jiao, W. Xu, D. Qiu and D. Zhu, *Adv. Mater.*, 2012, **24**, 932, DOI: 10.1002/adma.201104305.

16 E. Jang, A. Poosapati and D. Madan, *ACS Appl. Energy Mater.*, 2018, **1**, 1455, DOI: 10.1021/acsaem.7b00231.

17 X. Zhao, D. Madan, Y. Cheng, J. Zhou, H. Li, S. M. Thon, A. E. Bragg, M. E. DeCoster, P. E. Hopkins and H. E. Katz, *Adv. Mater.*, 2017, **29**, 1606928, DOI: 10.1002/adma.201606928.

18 D. Madan, X. Zhao, R. M. Ireland, D. Xiao and H. E. Katz, *APL Mater.*, 2017, **5**, 086106, DOI: 10.1063/1.4990139.

19 D. Madan, Z. Wang, A. Chen, R. Winslow, P. K. Wright and J. W. Evans, *Appl. Phys. Lett.*, 2014, **104**, 2012, DOI: 10.1063/1.4861057.

20 A. Chen, D. Madan, P. K. Wright and J. W. Evans, *J. Manuf. Syst.*, 2011, **21**, 104006, DOI: 10.1088/0960-1317/21/10/104006.

21 D. Madan, A. Chen, P. K. Wright and J. W. Evans, *J. Appl. Phys.*, 2011, **109**, 034904, DOI: 10.1063/1.3544501.

22 S. J. Kim, H. Choi, Y. Kim, J. H. We, J. S. Shin, H. E. Lee, M. W. Oh, K. J. Lee and B. J. Cho, *Nano Energy*, 2017, **31**, 258, DOI: 10.1016/j.nanoen.2016.11.034.

23 T. Varghese, C. Hollar, J. Richardson, N. Kempf, C. Han, P. Gamarachchi, D. Estrada, R. J. Mehta and Y. Zhang, *Sci. Rep.*, 2016, **6**, 6, DOI: 10.1038/srep33135.

24 T. Varghese, C. Dun, N. Kempf, M. Saeidi-Javash, C. Karthik, J. Richardson, C. Hollar, D. Estrada and Y. Zhang, *Adv. Funct. Mater.*, 2020, **30**, 1905796, DOI: 10.1002/adfm.201905796.

25 S. Shin, R. Kumar, J. W. Roh, D. S. Ko, H. S. Kim, S. I. Kim, L. Yin, S. M. Schlossberg, S. Cui, J. M. You, S. Kwon, J. Zheng, J. Wang and R. Chen, *Sci. Rep.*, 2017, **7**, 1, DOI: 10.1038/s41598-017-07654-2.

26 D. Ji, P. Liu, P. Im, S. Shin and J. Kim, *Adv. Funct. Mater.*, 2024, 2402144, DOI: 10.1002/adfm.202402144.

27 X. Lu, D. T. Morelli, Y. Xia, F. Zhou, V. Ozolins, H. Chi, X. Zhou and C. Uher, *Adv. Energy Mater.*, 2013, **3**, 342, DOI: 10.1002/aenm.201200650.

28 R. Chetty, A. Bali and R. C. Mallik, *J. Mater. Chem. C*, 2015, **3**, 12364, DOI: 10.1039/c5tc02537k.

29 K. Suekuni, K. Tsuruta, T. Ariga and M. Koyano, *Appl. Phys. Express*, 2012, **5**, 051201, DOI: 10.1143/APEX.5.051201.

30 K. Suekuni, K. Tsuruta, M. Kunii, H. Nishiate, E. Nishibori, S. Maki, M. Ohta, A. Yamamoto and M. Koyano, *J. Appl. Phys.*, 2013, **113**, 043712, DOI: 10.1063/1.4789389.

31 T. Barbier, P. Lemoine, S. Gascoin, O. I. Lebedev, A. Kaltzoglou, P. Vaqueiro, A. V. Powell, R. I. Smith and E. Guilmeau, *J. Alloys Compd.*, 2015, **634**, 253, DOI: 10.1016/j.jallcom.2015.02.045.

32 R. Chetty, D. S. Prem Kumar, G. Rogl, P. Rogl, E. Bauer, H. Michor, S. Suwas, S. Puchegger, G. Giester and R. C. Mallik, *Phys. Chem. Chem. Phys.*, 2015, **17**, 1716, DOI: 10.1039/c4cp04039b.

33 P. Banerjee, J. Huang, R. B. Ambade, E. Jang, M. Saeidi-javash, Y. Zhang and D. Madan, *Nano Energy*, 2021, **89**, 106482, DOI: 10.1016/j.nanoen.2021.106482.

34 J. Huang, R. B. Ambade, J. Lombardo, B. Brooks, A. Poosapati, P. Banerjee, M. Saeidi-Javash, Y. Zhang and D. Madan, *Appl. Mater. Today*, 2024, **37**, 102116, DOI: 10.1016/j.apmt.2024.102116.

35 E. Jang, P. Banerjee, J. Huang, R. Holley, J. T. Gaskins, M. S. Bin Hoque, P. E. Hopkins and D. Madan, *Electronics*, 2020, **9**, 1, DOI: 10.3390/electronics9030532.

36 P. Banerjee, E. Jang, J. Huang, R. Holley, S. Vadnala, A. Sheikh, A. Trivedi, K. Jackson, V. K. Homman and D. Madan, *J. Electron. Mater.*, 2021, **50**, 2840, DOI: 10.1007/s11664-021-08798-8.

37 D. Madan, Z. Wang, P. K. Wright and J. W. Evans, *Appl. Energy*, 2015, **156**, 587, DOI: 10.1016/j.apenergy.2015.07.066.

38 E. Jang, A. Poosapati, N. Jang, L. Hu, M. Duffy, M. Zupan and D. Madan, *Sci. Rep.*, 2019, **9**, 7869, DOI: 10.1038/s41598-019-44225-z.

39 E. Jang, P. Banerjee, J. Huang and D. Madan, *Appl. Energy*, 2021, **294**, 117006, DOI: 10.1016/j.apenergy.2021.117006.

40 R. B. Ambade, S. B. Ambade, G. Kumar Veerasubramani, K. H. Lee and T. H. Han, *J. Power Sources*, 2024, **608**, 234615, DOI: 10.1016/j.jpowsour.2024.234615.

41 S. B. Ambade, R. B. Ambade, W. Eom, S. H. Noh, S. H. Kim and T. H. Han, *Adv. Mater. Interfaces*, 2018, **5**, 1801361, DOI: 10.1002/admi.201801361.

42 A. Sarycheva and Y. Gogotsi, Raman Spectroscopy Analysis of the Structure and Surface Chemistry of Ti3C2Tx MXene, *Chem. Mater.*, 2020, **32**, 3480–3488, DOI: 10.1021/acs.chemmater.0c00359.

43 S. B. Ambade, L. A. Kesner, M. K. Abdel-Rahman, D. H. Fairbrother and Z. Rosenzweig, *ACS Appl. Nano Mater.*, 2023, **6**, 4898, DOI: 10.1021/acsanm.3c00666.

44 J. Diao, J. Yuan, Z. Cai, L. Xia, Z. Cheng, X. Liu and W. Ma, *Carbon*, 2022, **196**, 243, DOI: 10.1016/j.carbon.2022.04.078.

45 S. Kumar, S. Singh, P. K. Dhawan, R. R. Yadav and N. Khare, *Nanotechnol.*, 2018, **29**, 135703, DOI: 10.1088/1361-6528/aaa99e.

46 B. Anasori, M. R. Lukatskaya and Y. Gogotsi, *Nat. Rev. Mater.*, 2017, **2**, 1–17, DOI: 10.1038/natrevmats.2016.98.

47 S. H. Lee, W. Eom, H. Shin, R. B. Ambade, J. H. Bang, H. W. Kim and T. H. Han, *ACS Appl. Mater. Interfaces*, 2020, **12**, 10434–10442, DOI: 10.1021/acsami.9b21765.

666 | *J. Mater. Chem. A*, 2025, **13**, 654–668

This journal is © The Royal Society of Chemistry 2025

48 Y. Gogotsi and Q. Huang, *ACS Nano*, 2021, **15**, 5775, DOI: 10.1021/acsnano.1c03161.

49 K. Hantanasirisakul, M. Alhabeb, A. Lipatov, K. Maleski, B. Anasori, P. Salles, C. Leosakulrat, P. Pakawatpanurut, A. Sinitskii, S. J. May and Y. Gogotsi, *Chem. Mater.*, 2019, **31**, 2941, DOI: 10.1021/acs.chemmater.9b00401.

50 X. Lu, Q. Zhang, J. Liao, H. Chen, Y. Fan, J. Xing, S. Gu, J. Huang, J. Ma, J. Wang, L. Wang and W. Jiang, *Adv. Energy Mater.*, 2020, **10**, 1, DOI: 10.1002/aenm.201902986.

51 V. Karthikeyan, V. C. S. Theja, M. M. De Souza and V. A. L. Roy, *Phys. Status Solidi RRL*, 2022, **16**, 2011419, DOI: 10.1002/pssr.202100419.

52 R. Chetty, A. Bali, M. H. Naik, G. Rogl, P. Rogl, M. Jain, S. Suwas and R. C. Mallik, *Acta Mater.*, 2015, **100**, 266, DOI: 10.1016/j.actamat.2015.08.040.

53 D. J. James, X. Lu, D. T. Morelli and S. L. Brock, *ACS Appl. Mater. Interfaces*, 2015, **7**, 23623, DOI: 10.1021/acsami.5b07141.

54 F. Makin, F. Alam, M. A. Buckingham and D. J. Lewis, *Sci. Rep.*, 2022, **12**, 5627, DOI: 10.1038/s41598-022-08822-9.

55 D. S. P. Kumar, M. Ren, T. Osipowicz, R. C. Mallik and P. Malar, *Sol. Energy*, 2018, **174**, 422, DOI: 10.1016/j.solener.2018.08.080.

56 T. Rath, A. J. MacLachlan, M. D. Brown and S. A. Haque, *J. Mater. Chem. A*, 2015, **3**, 24155, DOI: 10.1039/c5ta05777a.

57 D. Zhang, J. Cao, X. Zhang, N. Insin, R. Liu and J. Qin, *ACS Appl. Energy Mater.*, 2020, **3**, 5949, DOI: 10.1021/acsaem.0c00863.

58 P. A. Fernandes, A. Shongalova, A. F. da Cunha, J. P. Teixeira, J. P. Leitão, J. M. V. Cunha, S. Bose, P. M. P. Salomé and M. R. Correia, *J. Alloys Compd.*, 2019, **797**, 1359, DOI: 10.1016/j.jallcom.2019.05.149.

59 D. Han, T. Han, C. Shan, A. Ivaska and L. Niu, *Electroanalysis*, 2010, **22**, 2001, DOI: 10.1002/elan.201000094.

60 D. A. Polvani, J. F. Meng, N. V. Chandra Shekar, J. Sharp and J. V. Badding, *Chem. Mater.*, 2001, **13**, 2068, DOI: 10.1021/cm000888q.

61 Z. Wu, X. Chen, E. Mu, Y. Liu, Z. Che, C. Dun, F. Sun, X. Wang, Y. Zhang and Z. Hu, *Adv. Electron. Mater.*, 2020, **6**, 1900735, DOI: 10.1002/aelm.201900735.

62 G. J. Snyder, A. H. Snyder, M. Wood, R. Gurunathan, B. H. Snyder and C. Niu, Weighted Mobility, *Adv. Mater.*, 2020, **32**, 1, DOI: 10.1002/adma.202001537.

63 D. P. Weller and D. T. Morelli, *J. Alloys Compd.*, 2017, **710**, 794, DOI: 10.1016/j.jallcom.2017.03.272.

64 U. V. Ghorpade, M. P. Suryawanshi, S. W. Shin, X. Wang, E. Jo, H. Bae, K. Park, J. S. Ha, S. S. Kolekar and J. H. Kim, *J. Mater. Chem. A*, 2018, **6**, 19798, DOI: 10.1039/c8ta07400c.

65 Z. Wang, A. Chen, R. Winslow, D. Madan, R. C. Juang, M. Nill, J. W. Evans and P. K. Wright, *J. Manuf. Syst.*, 2012, **22**, 094001, DOI: 10.1088/0960-1317/22/9/094001.

66 D. Madan, A. Chen, P. K. Wright and J. W. Evans, *J. Electron. Mater.*, 2012, **41**, 1481, DOI: 10.1007/s11664-011-1885-5.

67 D. Madan, Z. Wang, A. Chen, R. Juang, J. Keist, P. K. Wright and J. W. Evans, *ACS Appl. Mater. Interfaces*, 2012, **4**, 6117, DOI: 10.1021/am301759a.

68 D. Madan, Z. Wang, A. Chen, P. K. Wright and J. W. Evans, *ACS Appl. Mater. Interfaces*, 2013, **5**, 11872, DOI: 10.1021/am403568t.

69 H. Choi, Y. J. Kim, C. S. Kim, H. M. Yang, M. W. Oh and B. J. Cho, *Nano Energy*, 2018, **46**, 39, DOI: 10.1016/j.nanoen.2018.01.031.

70 X. Fan, E. D. Case, X. Lu and D. T. Morelli, *J. Mater. Sci.*, 2013, **48**, 7540, DOI: 10.1007/s10853-013-7569-1.

71 Y. Y. Li, X. Y. Qin, D. Li, J. Zhang, C. Li, Y. F. Liu, C. J. Song, H. X. Xin and H. F. Guo, *Appl. Phys. Lett.*, 2016, **108**, 3, DOI: 10.1063/1.4941757.

72 T. Barbier, S. Rollin-Martinet, P. Lemoine, F. Gascoin, A. Kaltzoglou, P. Vaqueiro, A. V. Powell and E. Guilmeau, *J. Am. Ceram. Soc.*, 2016, **99**, 51, DOI: 10.1111/jace.13838.

73 P. C. Li, G. M. Liao, S. R. Kumar, C. M. Shih, C. C. Yang, D. M. Wang and S. J. Lue, *Electrochim. Acta*, 2016, **187**, 616, DOI: 10.1016/j.electacta.2015.11.117.

74 G. Lawrie, I. Keen, B. Drew, A. Chandler-Temple, L. Rintoul, P. Fredericks and L. Grøndahl, *Biomacromolecules*, 2007, **8**, 2533, DOI: 10.1021/bm070014y.

75 J. A. Mielczarski, J. M. Cases, M. Alnot and J. J. Ehrhardt, *Langmuir*, 1996, **12**, 2519, DOI: 10.1021/la950589t.

76 G. H. Albuquerque, K. Kim, J. I. Lopez, A. Devaraj, S. Manandhar, Yi. Liu, J. Guo, C. Changa and G. S. Herman, *J. Mater. Chem. A*, 2018, **6**, 8682, DOI: 10.1039/C8TA00001H.

77 M. Tamilselvan and A. J. Bhattacharyya, *ACS Appl. Energy Mater.*, 2018, **1**, 4227, DOI: 10.1021/acsaem.8b00844.

78 D. S. Prem Kumar, S. Tippireddy, A. Ramakrishnan, K. H. Chen, P. Malar and R. C. Mallik, *Semicond. Sci. Technol.*, 2019, **34**, 035017, DOI: 10.1088/1361-6641/aafa31.

79 H. I. Tanaka, K. Suekuni, K. Umeo, T. Nagasaki, H. Sato, G. Kutluk, E. Nishibori, H. Kasai and T. Takabatake, *J. Phys. Soc. Jpn.*, 2016, **85**, 014703, DOI: 10.7566/JPSJ.85.014703.

80 J. Yang, Y. Zhang, Y. Zhang, J. Shao, H. Geng, Y. Zhang, Y. Zheng, M. Ulaganathan, Z. Dai, B. Li, Y. Zong, X. Dong, Q. Yan and W. Huang, *Small*, 2017, **13**, 1702181, DOI: 10.1002/smll.201702181.

81 Y. Zhang, C. Ma, W. He, C. Zhang, L. Zhou, G. Wang and W. Wei, *Prog. Nat. Sci.: Mater. Int.*, 2021, **31**, 501, DOI: 10.1016/j.pnsc.2021.07.003.

82 C. Lu, A. Li, G. Li, Y. Yan, M. Zhang, Q. Yang, W. Zhou and L. Guo, *Adv. Mater.*, 2021, **33**, 2008414, DOI: 10.1002/adma.202008414.

83 W. Bao, R. Wang, C. Qian, Z. Zhang, R. Wu, Y. Zhang, F. Liu, J. Li and G. Wang, *ACS Nano*, 2021, **15**, 16207, DOI: 10.1021/acsnano.1c05193.

84 Y. Cao, Y. Zhang, H. Chen, S. Qin, L. Zhang, S. Guo and H. Yang, *Adv. Funct. Mater.*, 2022, **32**, 2108574, DOI: 10.1002/adfm.202108574.

85 C. Gayner and Y. Amouyal, *Adv. Funct. Mater.*, 2020, **30**, 1, DOI: 10.1002/adfm.201901789.

This journal is © The Royal Society of Chemistry 2025

J. Mater. Chem. A, 2025, **13**, 654–668 | **667**

86 A. J. Minnich, M. S. Dresselhaus, Z. F. Ren and G. Chen, *Energy Environ. Sci.*, 2009, **2**, 466, DOI: **10.1039/b822664b**.

87 T. Alqahtani, M. D. Khan, D. J. Lewis, X. L. Zhong and P. O'Brien, *Sci. Rep.*, 2021, **11**, 1887, DOI: **10.1038/s41598-020-80951-5**.

88 K. H. Lim, M. Li, Y. Zhang, Y. Wu, Q. Zhou, Q. Wang, X. Yang, P. Liu, W. J. Wang, K. W. Wong, K. M. Ng, Y. Liu and A. Cabot, *J. Mater. Sci. Technol.*, 2024, **171**, 71, DOI: **10.1016/j.jmst.2023.07.008**.

89 L. D. Hicks and M. S. Dresselhaus, *Phys. Rev. B*, 1993, **47**, 12727, DOI: **10.1103/PhysRevB.47.12727**.

90 Y. P. Mamunya, V. V. Davydenko, P. Pissis and E. V. Lebedev, Electrical and thermal conductivity of polymers filled with metal powders, *Eur. Polym. J.*, 2002, **38**, 1887, DOI: **10.1016/S0014-3057(02)00064-2**.

91 H. J. Goldsmid and R. W. Douglas, *Br. J. Appl. Phys.*, 1954, **5**, 386, DOI: **10.1088/0508-3443/5/11/303**.

92 K. Ganesan, S. Ghosh, N. Gopala Krishna, S. Ilango, M. Kamruddin and A. K. Tyagi, *Phys. Chem. Chem. Phys.*, 2016, **18**, 22160–22167, DOI: **10.1039/C6CP02033J**.

93 X. Xiao, Q. Xu, S. Liang, H. Zhang, L. Ma, L. Hai and X. Zhang, *RSC Adv.*, 2022, **12**, 19091, DOI: **10.1039/d2ra02775e**.

94 C. R. O'Connor, M. A. van Spronsen, M. Karatok, J. Boscoboinik, C. M. Friend and M. M. Montemore, *J. Phys. Chem. C*, 2021, **125**, 10685–10692, DOI: **10.1021/acs.jpcc.1c01450**.

95 S. H. Park, S. Jo, B. Kwon, F. Kim, H. W. Ban, J. E. Lee, D. H. Gu, S. H. Lee, Y. Hwang, J. Kim, D. Hyun, S. Lee, K. J. Choi, W. Jo and J. S. Son, *Nat. Commun.*, 2016, **7**, 1, DOI: **10.1038/ncomms13403**.

96 O. Hellman and D. A. Broido, *Phys. Rev. B*, 2014, **90**, 1, DOI: **10.1103/PhysRevB.90.134309**.

97 C. W. Nan, G. Liu, Y. Lin and M. Li, *Appl. Phys. Lett.*, 2004, **85**, 3549, DOI: **10.1063/1.1808874**.

98 Y. Pei, H. Wang and G. J. Snyder, *Adv. Mater.*, 2012, **24**, 6125, DOI: **10.1002/adma.201202919**.

99 S. Tippireddy, R. Chetty, M. H. Naik, M. Jain, K. Chattopadhyay and R. C. Mallik, *J. Phys. Chem. C*, 2018, **122**, 8735, DOI: **10.1021/acs.jpcc.7b12214**.

100 C. Meng, C. Liu and S. Fan, *Adv. Mater.*, 2010, **22**, 535, DOI: **10.1002/adma.200902221**.

101 S. Ganguly, C. Zhou, D. Morelli, J. Sakamoto and S. L. Brock, *J. Phys. Chem. C*, 2012, **116**, 17431, DOI: **10.1021/jp3055608**.

102 S. I. Kim, H. A. Mun, H. S. Kim, S. W. Hwang, J. W. Roh, D. J. Yang, W. H. Shin, X. S. Li, Y. H. Lee, G. J. Snyder and S. W. Kim, *Science*, 2015, **348**, 109, DOI: **10.1126/science.aaa4166**.

103 M. N. Hang, I. L. Gunsolus, H. Wayland, E. S. Melby, A. C. Mensch, K. R. Hurley, J. A. Pedersen, C. L. Haynes and R. J. Hamers, *Chem. Mater.*, 2016, **28**, 1092, DOI: **10.1021/acs.chemmater.5b04505**.

104 S. Sengupta, S. B. Ambade, T. L. O'Keefe, F. Tawakalna, J. K. H. Orbeck, R. J. Hamers, Z. V. Feng, C. L. Haynes and Z. Rosenzweig, *Environ. Sci.: Nano*, 2024, **11**, 627, DOI: **10.1039/D3EN00382E**.

105 D. N. Williams, J. S. Saar, V. Bleicher, S. Rau, K. Lienkamp and Z. Rosenzweig, *ACS Appl. Bio Mater.*, 2020, **3**, 1097, DOI: **10.1021/acsabm.9b01045**.

106 T. S. Mathis, K. Maleski, A. Goad, A. Sarycheva, M. Anayee, A. C. Foucher, K. Hantanasirisakul, C. E. Shuck, E. A. Stach and Y. Gogotsi, *ACS Nano*, 2021, **15**, 6420, DOI: **10.1021/acsnano.0c08357**.

668 | *J. Mater. Chem. A*, 2025, **13**, 654–668

This journal is © The Royal Society of Chemistry 2025